Noname manuscript No.
(will be inserted by the editor)

Hyperbolic systems of conservation laws in gravity-driven, particle-laden thin-film flows

A. Mavromoustaki* · **A. L. Bertozzi**
520 Portola Plaza, Mathematical Sciences
University California, Los Angeles

June 13, 2013

Abstract Our study focuses on gravity-driven, particle-laden flows which are pertinent to a wide range of industrial and geophysical settings in which transport of suspensions occur. In the present study we employ a previously derived model [1] which uses the lubrication approximation to describe particle-laden films on an incline. The model consists of a coupled system of hyperbolic conservation laws for the interface position and the particle concentration. While it has been shown that the model compares well quantitatively with experiments, it lacks analysis. The objectives of this paper focus on the study of the Riemann problem for this system of conservation laws and how the results relate to experiments. We investigate the governing system analytically and numerically; the equations exhibit rich mathematical structures including double-shock wave solutions, rarefaction waves and singular shocks.

Keywords Lubrication · particle-laden flow · hyperbolic system of conservation laws · numerical modeling · classical shocks · singular shocks · rarefaction waves

*Corresponding author
Email: am503@math.ucla.edu
Tel.: +1-310-825-8525

1 Introduction

Thin films occur in fluid flows over a vast range of length scales and are pertinent to many engineering applications (such as microfluidics, coating flows, heat transfer processes) as well as geophysics (such as mud slides, debris flows, oil and gas applications). Further, many areas of biophysics and medical physics have advanced through thin films, such as in tear-film rupture and surfactant replacement therapy in neonates. Due to their wide range of applications, thin films have received substantial attention in the literature in the past few decades [2–5]. Mixtures of fluid and particles, though extremely relevant in geophysical applications both in small and large scales, have received far less attention. The presence of solid particles in slurries and their efficient handling is central to many of the above-mentioned applications which renders the understanding of the dynamics of these flows extremely important. The flow of a viscous fluid laden with small, spherical particles and flowing down an incline under the action of gravity will be the subject of the present work.

While the behavior of a single particle in Stokes flow is well understood, the settling and resuspension of large volumes of particles in a slurry is not; consequently, one resorts to empirical or semi-empirical correlations to model such processes. Some of the earliest work on the subject investigated gravitational settling/sedimentation of a uniform suspension of particles in a quiescent bulk fluid [6–8]. Richardson and Zaki [7] carried out a series of experiments to suggest an expression for the drag force; this expression showed good agreement with theory. In the current study, the interest lies in the gravitational transport of particles within a thin film of viscous oil. It has been shown experimentally that particle-laden, thin-film slurries falling under gravity develop three distinct regimes in the presence of contact lines [9]; these are shown in Fig. 1.

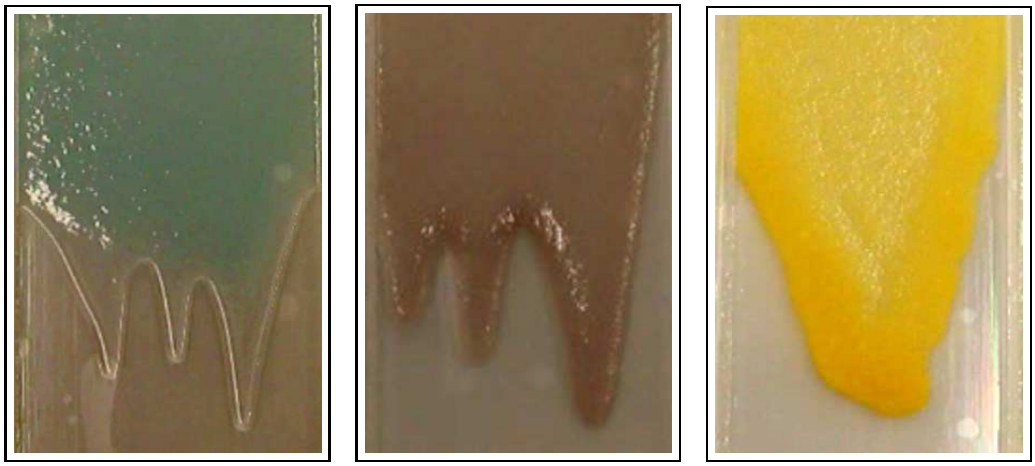

(a) (b) (c)

Fig. 1 Flow regime patterns emerging from a fixed volume of silicon oil laden with small ($\sim 300\,\mu m$), negatively buoyant glass beads. In (a)-(c), the particle volume fraction is set as 0.25, 0.35 and 0.5 corresponding to the 'settled', 'well-mixed' and 'ridged' regime, respectively. In the 'settled' regime, clear fluid flows over the particle-rich fluid while in the 'ridged' regime, the particles accumulate at the front indicated by the darker yellow color in panel (c). The middle panel shows an intermediate regime where the particles remain well mixed in the fluid. The plane angle of inclination is set to 30^o in all panels. The images show the patterns at their fully developed state. The experiments were run in the Applied Mathematics Laboratory at University California, Los Angeles (UCLA).

At low concentrations and angles of inclination, the particles tend to settle rapidly thus allowing clear fluid to flow over them. The clear fluid front then undergoes a fingering instability as expected from previous work on the stability of single, particle-free layers [10, 11]. At large particle concentrations and angles, the particles advance towards the front of the flow and accumulate to form a particle-rich ridge which suppresses the fingering. A transient regime exists at intermediate concentrations and angles wherein the particles appear to remain well mixed within the slurry while the front is seen to be unstable to fingering formation. Following the work of Murisic *et al.* [1] we henceforth refer to the three regimes as 'settled' [see Fig. 1(a)], 'well-mixed' [see Fig. 1(b)] and 'ridged' [see Fig. 1(c)]. While the study of gravity-driven, clear, thin films is rather straightforward, the addition of particles in the fluid complicates matters through the actions of particles settling due to gravity, and their resuspension, the latter induced by shear. These processes are further complicated by the different time scales they act upon; various system parameters such as the plane angle of inclination, particle size and density affect these and need to be accounted, for the accurate prediction of the flow dynamics.

Existing models [9, 12] use the lubrication approximation to simplify the three-dimensional particle transport, continuity and Stokes equations to derive a coupled system of equations to describe the evolution of the free surface and particle concentration. It is noted that the Stokes equations are modified to account for the effect of the particles on the slurry density and viscosity. The model employed in [9, 12] accounts for the effects of gravity, capillarity and hindered settling. The solutions were found to approach the 'ridged' regime behavior but failed to capture the separation between the particle-free and particle-rich regions observed in the 'settled' regime. In the subsequent studies of Cook [13] and Cook *et al.* [14], it was suggested that shear-induced migration phenomena are important and should be included in the dominant physics of the problem. The lubrication models derived in the above-mentioned studies assume that transport due to shear or settling occurs rapidly in the normal direction such that these processes depend solely on the axial flow direction and time. The most recent model [1, 15] reviews the important flow dynamics and the time scales within which they occur. It employs the so-called 'equilibrium' theory whereby it is assumed that the fluxes accounting for gravitational settling and resuspension due to shear-induced migration are balanced. This leads to a coupled system of ODEs which confirms the existence of two separate regimes - one wherein all the particles settle to the substrate and a second one wherein the particles are distributed throughout the film thus reaching the free surface. The ODE solutions indicate that there exists an unstable state which corresponds to the transient regime observed at intermediate particle concentrations and angles. Further, due to the small thickness of the film, any particle motion in the normal direction, is said to occur fast compared to the flow direction. Extensive experimental work has been done in [1] which shows excellent agreement with the equilibrium theory employed in the model. In the studies by Murisic *et al.* [1, 15], the evolution equations are solved numerically and compared with physical experiments in the settled regime.

Motivated by the good agreement between theory and experiments, we focus our analysis on the model derived in [1, 15]. The model consists of two coupled, hyperbolic conservation laws which describe the evolution of the position of the interface and the particle volume fraction. This paper presents a detailed analysis of the Riemann problem where we identify several types of solutions that emerge, including classical shock solutions, rarefaction waves and singular shocks. Such solutions have been shown to exist for other fluid systems in the literature such as the flow of clear, thin films down an incline [11, 16]. One-dimensional solutions show that the flow develops a traveling-wave solution given by a compressive shock, which moves with constant velocity; the latter is given by a characteristic speed which satisfies the Rankine-Hugoniot jump condition. Bertozzi *et al.* [17] investigated the flow of a fluid climbing up an inclined plane along surface tension gradients, created by an imposed temperature gradient along the interface and against the action of gravity. In the presence of both gravitational and surface tension gradient effects, the authors conclude that there exist several traveling-wave solutions depending on

the initial thickness of the film. These include solitary compressive shocks and double-shock waves comprised of compressive and undercompressive solutions. A further increase of the film thickness showed that the flow does not develop traveling-wave solutions; instead, undercompressive-rarefaction waves form at the interface. Similar dynamics are observed in particle-laden flows where, as one might expect, the complexity between the various competing forces increases substantially.

This paper is organized as follows: in Section 2, we outline the details of the theoretical model employing the assumptions based on the disparity of time scales of the various physical processes and the competition between the forces acting on the slurry as a result of the dominant physical effects present in the experimental setting. In Section 3, we discuss the shock dynamics theory as applied to the hyperbolic system of PDEs which describe the spatio-temporal evolution of the slurry flow. Numerical solutions are presented and the effect of the most important system parameters is outlined. Further, we discuss the nature of the shocks and wave solutions found numerically and their relevance to physical observations. Finally, concluding remarks are given in Section 4.

2 Theoretical model

2.1 Two-phase equations

In this subsection, we review the model derived in the work of Murisic *et al.* [1, 15]. We consider the spreading of a thin fluid laden with spherical, mono-disperse particles of volumetric concentration ϕ. The fluid is assumed to be incompressible of density $\rho_{_L}$ and viscosity $\mu_{_L}$ while the particles are assumed to be rigid, noncolloidal and negatively buoyant. The density of the particles is denoted by $\rho_{_P}$. The subscripts 'P' and 'L' refer to 'particle' and 'liquid' properties, respectively. The slurry, composed of a well-mixed mixture of fluid and particles, flows down a rectangular incline, under the action of gravity. The incline has been prewetted by a thin, particle-free fluid of uniform thickness, h_+. The equations governing the fluid dynamics are given by the three-dimensional continuity and Stokes equations [see Eqs. (1) and (2)] for an incompressible fluid.

$$\nabla \cdot \mathbf{u} = 0, \tag{1}$$

$$\nabla p - \nabla \cdot \left[\mu(\phi)\left(\nabla \mathbf{u} + \nabla \mathbf{u}^T\right)\right] = \rho(\phi)\mathbf{g}; \tag{2}$$

where $\rho(\phi) = [\rho_{_P}\phi + \rho_{_L}(1-\phi)]$ and $\mathbf{u} = (u, v, w)$, where u, v and w represent the axial, transverse and normal components of the velocity field, respectively. The effective viscosity is modelled using the Krieger-Dougherty relation [18, 19] given as $\mu(\phi) = \mu_{_L}\,(1 - \phi/\phi_{\max})$. In order to take into account the presence of particles, the Stokes equations are modelled using the so-called effective suspension density, $\rho(\phi)$ and viscosity, $\mu(\phi)$. It is noted that the viscous forces in this setting are dominant compared to inertial forces, hence any contributions due to inertia are ignored. For the particle volume fraction, we use a transient, particle transport equation [see Eq. (3)] which takes into account the flow of particles due to advection and flux gradients; the latter being a result due to the combined effect of contributions due to particle collisions and changes in the effective density and viscosity.

$$\phi_t + \mathbf{u} \cdot \nabla\phi + \nabla \cdot \mathbf{J} = 0, \tag{3}$$

with

$$\mathbf{J} = \mathbf{J}_{grav} + \mathbf{J}_{coll} + \mathbf{J}_{visc}; \tag{4}$$

where $\mathbf{J}$ represents the total flux of particles comprised of flux due to gravity, $\mathbf{J}_{grav}$, shear-induced migration as a result of particle collisions, $\mathbf{J}_{coll}$ and viscosity gradients, $\mathbf{J}_{visc}$, given by Eqs. (5) below;

$$\begin{aligned} \mathbf{J}_{grav} &= \frac{d^2\phi(\rho_{_P} - \rho_{_L})}{18\mu_{_L}} f_s(\phi)\mathbf{g}, \\ \mathbf{J}_{coll} &= -\frac{K_c d^2}{4}\left(\phi\nabla\dot{\gamma} + \phi\dot{\gamma}\nabla\phi\right), \\ \mathbf{J}_{visc} &= -\frac{K_v d^2}{4\mu}\phi^2\dot{\gamma}\mu_\phi\nabla\phi. \end{aligned} \tag{5}$$

In Eqs. (5), d denotes the particle diameter, $\dot{\gamma}$ is the shear rate, $f_s(\phi)$ describes hindered particle settling due to gravity, defined later by Eq. (11), while K_c and K_v are empirical constants associated with the shear-induced migration arising from changes in the particle volume fraction and the effective suspension viscosity; these are taken as $K_c = 0.41$ and $K_v = 0.62$ [1, 20]. Equations (1)-(3) are solved subject to boundary conditions applied at the wall, located at $z = 0$ and at the free surface, $z = h(x, y, t)$. These correspond to the no-slip and no-penetration boundary condition at the wall and the tangential and normal stress balances at the free surface. The motion of the fluid at the free surface is described through the kinematic boundary condition given by

$$\frac{D}{Dt}\Big[z - h(x, y, t)\Big] = 0, \tag{6}$$

where D/Dt represents the material derivative. Finally, we impose no-flux boundary conditions at the wall and free surface for the particles

$$\mathbf{J} \cdot \mathbf{n} = 0; \tag{7}$$

we note that, in the current model, the particles do not attach to the free surface.

2.2 Equilibrium model

For the purposes of the current paper, we assume that the plane is of infinite width such that any changes in the flow in the transverse (y-direction) are negligible. Hence, we consider the dynamics in the axial and normal directions only, such that $\nabla = (\partial_x, 0, \partial_z)$ and $\mathbf{u} = (u, 0, w)$.

The governing equations are rendered dimensionless through the following scalings,

$$\begin{gathered} (x, y) = L(\tilde{x}, \tilde{y}), \quad (z, h) = H(\tilde{z}, \tilde{h}), \\ (u, v) = U(\tilde{u}, \tilde{v}), \quad w = (\epsilon U)\tilde{w}, \quad t = (L/U)\tilde{t}, \quad p = P\tilde{p}, \\ \dot{\gamma} = (U/H)\tilde{\dot{\gamma}}, \quad \phi = \Phi\tilde{\phi}, \end{gathered} \tag{8}$$

where the quantities shown with a tilde are dimensionless; L and H are the typical length scales for the length of the plane (in the x-direction) and the thickness of the film (in the z-direction), respectively, $\epsilon \equiv H/L$ is the lubrication parameter while U and P are the characteristic scales for the velocity and pressure, respectively. The dominant mechanism driving the flow is attributed to gravity, hence, a balance between gravity and the deviatoric stress terms yields the velocity scale as $U \equiv \rho_{_L} g \sin\alpha H^2/\mu_{_L}$ while, for negligible inertia flows, the appropriate scaling for the pressure is $P \equiv \mu_{_L} UL/H^2$. It is noted that, in the lubrication approximation, the shear rate, $\dot{\gamma}$ scales as $\sim \frac{\partial u}{\partial z}$ hence the choice of the U/H

scale in Eqs. (8). Finally, Φ denotes a typical particle volume concentration which, for simplicity, is taken to be equal to unity.

We introduce the aforementioned scalings (8) into the governing equations and boundary conditions given by Eqs. (1)-(7) which yield a set of dimensionless, leading order equations. In the lubrication approximation, the flow of the fluid is described by

$$\sigma_z = -(1 + \rho_s \phi), \tag{9}$$

where $\rho_s = (\rho_P - \rho_L)/\rho_L$ and we have used $\sigma = \mu(\phi) u_z$. Next, we nondimensionalize Eq. (3) through the scalings (8) which yields the following dimensionless particle transport equation,

$$\begin{aligned} \phi_t + u\phi_x + w\phi_z = &-\frac{d^2 \rho_s}{18H^2}\left[\left(\phi f_s(\phi)\right)_x + \epsilon^{-1} \left(\phi f_s(\phi) \cot\alpha\right)_z \right] \\ &+ \frac{K_c d^2}{4H^2}\left[\epsilon \left(\phi^2 \dot{\gamma}_x + \phi \dot{\gamma} \phi_x \right)_x + \epsilon^{-1} \left(\phi^2 \dot{\gamma}_z + \phi \dot{\gamma} \phi_z \right)_z \right] \\ &+ \frac{K_v d^2}{4H^2}\left[\epsilon \left(\frac{\phi^2}{\mu(\phi)} \dot{\gamma} \frac{d\mu}{d\phi} \phi_x \right)_x + \epsilon^{-1} \left(\frac{\phi^2}{\mu(\phi)} \dot{\gamma} \frac{d\mu}{d\phi} \phi_z \right)_z \right], \end{aligned} \tag{10}$$

where, following Murisic *et al.* [1,15], the dimensionless hindrance settling function implemented in the model is defined as

$$f_s(\phi) = (1 - \phi)/\mu(\phi). \tag{11}$$

We define the ratio between the particle diameter, d, and the typical height of the film, H, as $\eta \equiv d/H$. Here, we note that, while η may range from 0 (as $d \to 0$) to 1 (as $d \to H$), due to the assumptions made in deriving our theoretical model, we demand that the value of η does not approach the two extrema. For very small d, the particle distribution approaches that of a colloid dispersed in a fluid whose dynamics cannot be captured with the particle transport equation employed. The other extreme, i.e. as d approaches the height of the slurry thickness is considered impractical as it renders the continuum assumption to break down. The latter allows for the particle properties to be defined continuously, from one point to the next as opposed to considering each particle individually. To ensure that η is defined within these physically realizable limits, we demand that the square of the ratio, η^2 remains within $\epsilon << \eta^2 << 1$. As used in the derivation of the model in the work of Murisic *et al.* [15] we introduce the following scaling in the particle transport equation

$$\eta^2 = \epsilon^\beta, \quad \text{with} \quad 0 < \beta < 1. \tag{12}$$

Substituting Eqs. (11) and (12) in Eq. (10) and, given that $0 < \beta < 1$, the leading order terms are of $\mathcal{O}(\epsilon^{\beta-1})$; therefore, in leading order, the particle transport equation is given by

$$0 = \frac{\rho_s \cot\alpha}{18\phi_{\max}^2} \frac{d}{dz}\left[\phi(1-\phi)(\phi_{\max} - \phi)^2 \right] + \frac{K_c}{4} \frac{d}{dz}\left[\phi \frac{d}{dz}\left(\phi \frac{du}{dz} \right) \right] + \frac{K_v}{2} \frac{d}{dz}\left[\left(\frac{\phi^2}{\phi_{\max} - \phi} \right) \frac{du}{dz} \frac{d\phi}{dz} \right]; \tag{13}$$

where we have substituted $\dot{\gamma} = du/dz$, which is true in leading order. We note that the terms associated with temporal evolution and advection are of higher order, and do not appear in Eq. (13); thus, the latter represents an ordinary differential equation which can be integrated with respect to z. Upon integrating and employing zero-flux boundary conditions at $z = 0$, the particle transport equation is expressed as

$$0 = \sigma\phi' \left(1 + \frac{\phi}{\phi_{\max} - \phi} C_1 \right) - \phi(C_2 + 1) + C_2 - \rho_s \phi^2; \tag{14}$$

note we have used Eq. (9) to eliminate σ_z while, $C_1 = 2(K_v - K_c)/K_c$ and $C_2 = 2\rho_s \cot\alpha/9K_c$.

The model imposes a separation of time scales, emerging from the physics of the flow in the axial and normal directions. Attributed to the small thickness of the film, the flow dynamics in the normal direction is considered to be fast compared to the flow in the axial direction. This allows for an order-by-order analysis wherein the solutions to the leading order equations describe the shear stress and concentration distribution in the z-direction which, in turn, yield information on the velocity profile. The system of ODEs derived in Subsec. 2.2 given by Eqs. (9) and (14) are henceforth referred to as the 'equilibrium equations'. As shown in the literature [1, 13, 15], the ODE solutions constitute a family of curves parametrized by the total volume of particles present within the fluid film, ϕ_0 (defined below). Before proceeding, since the equilibrium equations are explicitly independent of the axial flow direction and time, it is also convenient to remove their implicit dependence [present through $h(x,t)$], by rescaling the normal direction, z. We introduce a new variable z^* which allows the normalization of z by h, defined as $z^* = z/h$. The equilibrium equations are rewritten as follows

$$\tilde{\sigma}' = -(1 + \rho_s\tilde{\phi}), \tag{15}$$

$$\tilde{\phi}' = \frac{\tilde{\phi}(1+C_2) + \rho_s\tilde{\phi}^2 - C_2}{\tilde{\sigma}\left(1 + C_1\frac{\tilde{\phi}}{\phi_{\max}-\tilde{\phi}}\right)}; \tag{16}$$

where the primes denote differentiation with respect to z^*. Here, we use the tilde decoration to indicate that the quantities employ the z^* scaling. The z-averaged particle volume fraction is given by $\phi_0 = \int_0^1 \tilde{\phi}\, dz^*$ defined within $0 \le \phi_0 \le \phi_{\max}$.

The system of ODEs is solved numerically subject to appropriate boundary conditions (refer to [1,15] for details on the numerical method employed). Figure 2(a) shows that the ODE solutions are represented by a family of curves parametrized by ϕ_0. The value of ϕ_0 is critical in dictating whether the particle concentration favors settling such that, as $z^* \to 1$, $\phi \to 0$ or, whether the particles will remain suspended in the fluid such that, as $z^* \to 1$, $\phi \to \phi_{\max}$, where $\phi_{\max}$ denotes particle maximum packing. This behavior is clearly depicted in Fig. 2(a) where the bottom part of the graph represents the 'settling' behavior while the top part represents a different regime which, for reasons evident through our experimental and numerical simulations, we refer to as 'ridged' or 'particle-rich' regime. The bottom part of the figure indicates that for low ϕ_0, the particles settle up to a certain height in the slurry which is lower than its thickness thus the top part of the fluid film remains particle-free. This is contrasted with the solutions shown in the upper part of the figure, which demonstrate that for high enough ϕ_0, there exist particle-rich regions throughout the fluid film. These ODE solutions suggest that there exists an unstable, flat state between the two regimes which is independent of variations in z^* i.e. when $\phi' = 0$. It is possible to calculate the critical particle volume fraction, ϕ_c [shown with a black, horizontal line in Fig. 2(a)] which represents this unstable flat state, through the system of ODEs yielding a relationship between ϕ_c and system constants C_2 and ρ_s,

$$\phi_c = \frac{-(1+C_2) + \sqrt{(1+C_2)^2 + 4\rho_s C_2}}{2\rho_s}. \tag{17}$$

The velocity profile may then be numerically constructed through the definition of the shear stress which rearranged yields $\tilde{u}(z^*) = \int_0^1 (\tilde{\sigma}/\tilde{\mu})\, dz^*$. We obtain the velocity distribution as a function of z^* by applying the no-slip condition at $z^* = 0$. This is shown in Fig. 2(b) for a ϕ_0 value equal to the critical point of transition, corresponding to the flat, horizontal line in the same figure in panel (a). We observe that the velocity distribution approaches a parabolic profile, as expected from particle-free, thin-film flow dynamics and satisfies the no-slip and no-shear conditions at the wall and free surface,

respectively. We note that the exact shape of the profile depends on the initial particle concentration and the relation employed to describe the effective viscosity of the slurry.

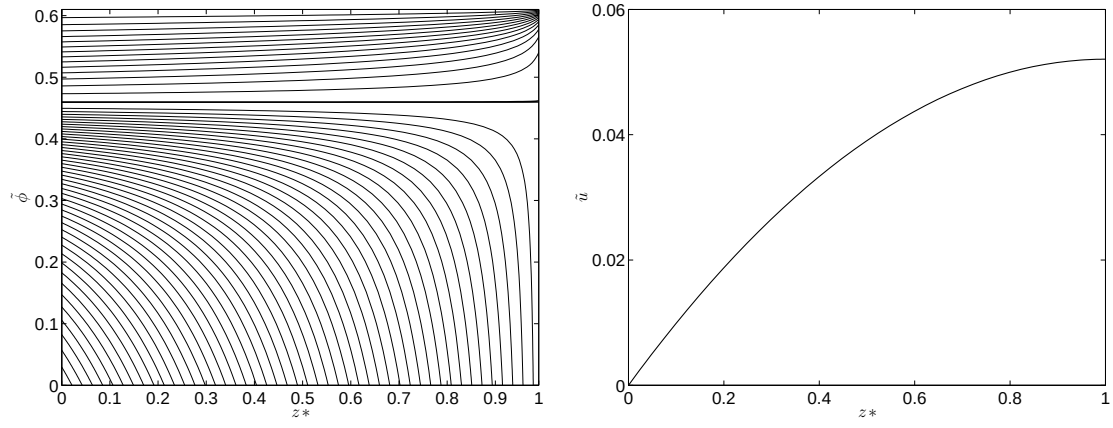

(a) (b)

Fig. 2 (a) Family of curves parametrized by ϕ_0 representing solutions to the system of ODEs given by Eqs. (15) and (16). The solutions depict the relationship of the particle volume fraction $\tilde{\phi}$ as a function of the rescaled normal direction z^*. They are obtained using a fourth-order, Runge-Kutta numerical scheme satisfying no-shear at the free surface; the latter is ensured through shooting method. The thick, horizontal line represents the unstable flat state solution which may be obtained analytically using Eq. (17) for given C_2 and ρ_s; here, it has been calculated as $\phi_c = 0.459$. (b) Velocity distribution for the critical particle concentration value, $\phi_c = 0.459$.

3 Hyperbolic system of PDEs

In the work of Murisic *et al.* [15], the authors focused on the numerical solution of the transport equation for low particle concentrations for which the evolution of the slurry is characterized by the 'settled' regime. As mentioned in Subsec. 2.2 , the ODE solutions prescribe the distribution of the particle concentration and ultimately the velocity profile of the slurry in the normal direction as a result of the balanced settling and resuspension forces. Using the kinematic boundary condition (6), and by moving on the next order in the particle transport equation, we obtain a system of conservation laws in terms of the dependent, conserved variables, $\boldsymbol{U} = (h, h\phi_0)$:

$$\boldsymbol{U}_t + \boldsymbol{F}_x = \boldsymbol{0}; \tag{18}$$

where $\boldsymbol{F} = (F, G)$ denotes the flux vector; F and G denote the fluxes of the film and particle equation, respectively and defined as

$$F = h^3 \int_0^1 \tilde{u}\, dz^* = h^3 f(\phi_0); \tag{19}$$

$$G = h^3 \int_0^1 \tilde{u}\tilde{\phi}\, dz^* = h^3 g(\phi_0). \tag{20}$$

Note that through the z^* scaling, it is possible to write down the fluxes as the product of a function of h and a function of ϕ_0; this is useful as the latter function bears no explicit dependence on h.

Upon expanding the flux terms, Eq. (18) is rewritten as

$$\boldsymbol{U}_t + J(\boldsymbol{U})\boldsymbol{U}_x = \boldsymbol{0}, \tag{21}$$

where $J(\boldsymbol{U})$ is the Jacobian matrix of the fluxes given by the column vector $\boldsymbol{F}$. The system of conservation laws given by Eq. (21) is hyperbolic if $J(\boldsymbol{U})$ has 2 real eigenvalues, λ_1, λ_2 and it is *strictly* hyperbolic if they are distinct such that $\lambda_1 < \lambda_2$. The Jacobian matrix is defined as in Murisic *et al.* [15]

$$J(\boldsymbol{U}) = h^2 \begin{pmatrix} 3f - \phi_0 f' & f' \\ 3g - \phi_0 g' & g' \end{pmatrix}, \tag{22}$$

where the primes denote differentiation with respect to ϕ_0. It is noted that the Jacobian matrix in (21) is obtained in terms of the conserved variables and then reconstructed in (22) in terms of the primitive variables, h and ϕ_0. The equations describing the transport system for our physical problem are found to be hyperbolic within the entire range of physically realistic values for ϕ_0, i.e. $0 \leq \phi_0 \leq \phi_{\max}$, as indicated in [15].

We now look at the Riemann problem for the 2×2 system of conservation laws, namely the solution corresponding to initial conditions separated by a jump discontinuity at $x = 0$:

$$\boldsymbol{U}(x, 0) = \begin{cases} \boldsymbol{U}_- & \text{if } x < 0, \\ \boldsymbol{U}_+ & \text{if } x > 0, \end{cases} \tag{23}$$

where $\boldsymbol{U}_-$ and $\boldsymbol{U}_+$ are given constants and represent the left and right states of $\boldsymbol{U}$. A schematic represenation showing the initial conditions for the film height is shown in Fig. 7.

3.1 Shocks and rarefaction waves theory

A shock solution must satisfy the *Rankine-Hugoniot* formula [21]; for the shock speed, s:

$$s = \frac{F_- - F_+}{h_- - h_+}, \quad s = \frac{G_- - G_+}{(h\phi_0)_- - (h\phi_0)_+}. \tag{24}$$

Here, F_-, G_- represent the fluxes evaluated at h_- and $(h\phi_0)_-$ and, similarly, F_+, G_+ denote the fluxes evaluated at h_+ and $(h\phi_0)_+$. Equations (24) must be satisfied across any discontinuity that exists between arbitrary upstream and downstream states. Note that with specified left and right states, in general, (24) is over-determined and will not have a solution. For a 2×2 system of conservation laws, we look for a two-wave solution comprised of either rarefactions or shocks. We focus on the shocks case first.

We follow the analysis carried out by Cook *et al.* [12] to identify all the possible shock wave connections to the system of equations presented in the current paper. Note that the theoretical model used in [12] was different to the one used in this paper. The Cook model employed a closed form for the fluxes, without incorporating all the relevant physics and it did not give quantitative agreement with the experiments. The current model is more challenging as it does not have closed formulae for the fluxes. Let us assume we fix the left states h_- and $(h\phi_0)_-$; there must exist certain right states h_+ and $(h\phi_0)_+$ for which the two relations in (24) are equal. The shock speed may be eliminated in Eqs. (24) to give

$$(F_- - F_+)[(h\phi_0)_- - (h\phi_0)_+] - (G_- - G_+)(h_- - h_+) = 0; \tag{25}$$

now, from (25), we are left with one degree of freedom which allows us to choose one of the unknown states, e.g. h_+, and solve for the second one, e.g. $(h\phi_0)_+$. The corresponding value of the unknown right

state ensures that the jump conditions are satisfied yielding a possible solution to the problem posed. Repeating the calculation for a range of right states for one of the variables gives a one-parameter family of solutions, henceforth referred to as the 'Rankine-Hugoniot locus' on the $(h, h\phi_0)$ plane showing the possible right states, that satisfy (25), given a set of known left states. Figure 3 shows the locus for the case where one set of the fixed states in Eq. (23) are chosen as $h_{_} = 1$ and $(h\phi_0)_{_} = 0.3$; note that, for practicality, the locus is shown on the (h, ϕ_0) plane. The locus shows all possible shock connections that can be connected to arbitrary $\boldsymbol{U}$ through the fixed state (1,0.3) via both 1-shock connections, if (1,0.3) is an upstream state or, 2-shock connections, if (1,0.3) is a downstream state.

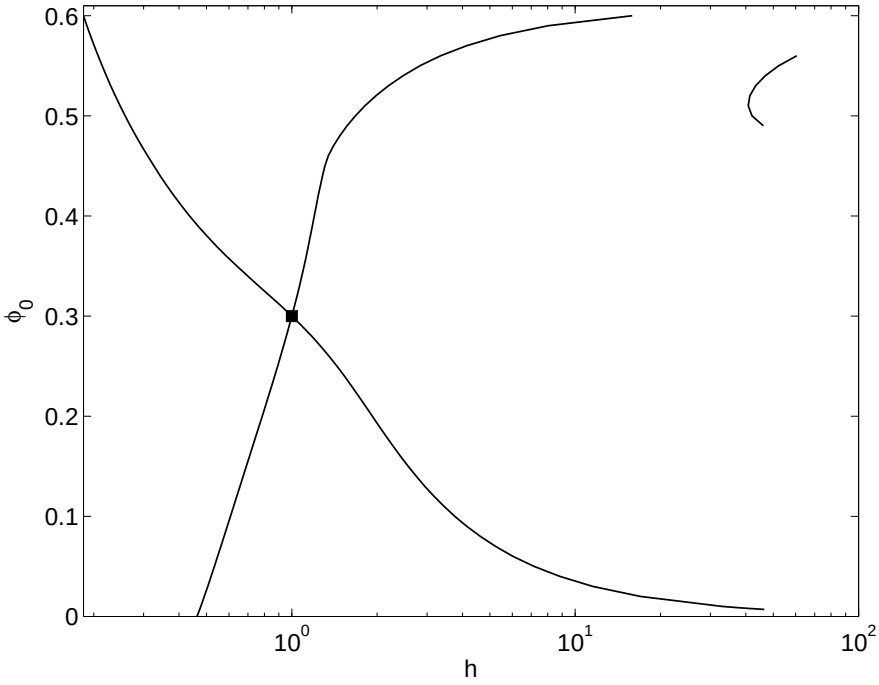

Fig. 3 Phase diagram showing the Rankine-Hugoniot locus calculated using Eq. (25). The locus shows all possible 1-shock and 2-shock connections from the fixed state chosen as $h_{_} = 1$ and $(\phi_0)_{_} = 0.3$ (the fixed states are indicated by the square marker).

We investigate what connections, if any, exist for given left and right states. This is achieved by plotting the Rankine-Hugoniot locus for two sets of fixed states, one representing the upstream states and a second representing the downstream states. If the connection curves generated from each given set of fixed states intersect, then a shock connection exists between the left and the right states via an intermediate state indicated by the point of intersection; this is shown in Figs. 4 and 5. Figure 4 shows all possible connections from an upstream state (solid lines) and a downstream state (dashed lines) including the points of intersection. Figure 5 shows all possible connections from an upstream state (solid line) and 2-shock connections yielding intersecting points with two downstream states. It is possible that the Rankine-Hugoniot locus exhibits multiple points of intersection - see, for example, Fig. 4. In such cases the solution is obviously not unique; in numerical simulations however we observe that the initial profiles evolve into a double-shock where a unique set of intermediate states connect the preset left and right states (see, for example, Fig. 8). We therefore need to identify whether the shock

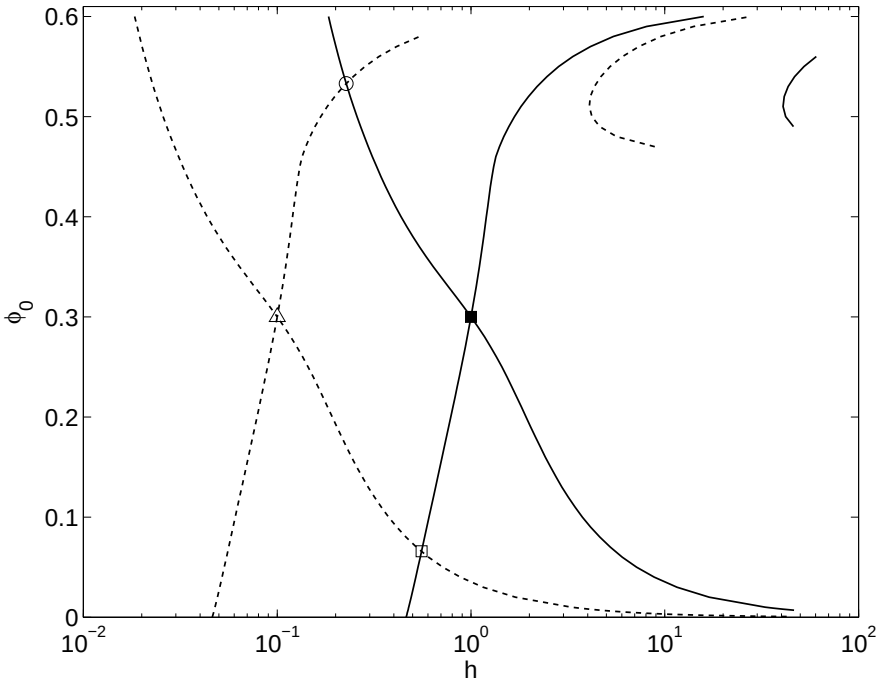

Fig. 4 The Rankine-Hugoniot locus calculated using Eq. (25) showing all possible shock connections (solid lines) from an upstream state $(h_{_-}, (\phi_0)_{_-}) = (1, 0.3)$ (■) and all possible shock connections (dashed lines) from a precursor state $(h_{_+}, (\phi_0)_{_+}) = (0.1, 0.3)$ (△). The intersections points show the possible intermediate states which are calculated as $(h_{_i}, (\phi_0)_{_i}) = (0.56, 0.065)$ (□) and $(h_{_i}, (\phi_0)_{_i}) = (0.23, 0.53)$ (◯).

connections given by the Rankine-Hugoniot locus are in fact *admissible*. Admissible solutions to systems like Eq. (18) are unique, weak solutions and are said to satisfy the following *entropy conditions* [21] for the k-characteristics:

$$\lambda_k(\boldsymbol{U}_{_-}) > s_k > \lambda_k(\boldsymbol{U}_{_+}), \quad \lambda_{k-1}(\boldsymbol{U}_{_-}) < s_k < \lambda_{k+1}(\boldsymbol{U}_{_+}); \tag{26}$$

where $1 \leq k \leq 2$ and λ denotes the eigenvalue of the Jacobian matrix defined by Eq. (22). Here, the subscripts '$-$' and '$+$' refer to upstream and downstream states, respectively. For $k = 1$, we are interested in the first shock or '1-shock' connecting the upstream (left) state to the intermediate states moving with speed s_1 while for $k = 2$, we are concerned with the second shock or '2-shock' connecting the intermediate states to the downstream (right) states, moving with speed s_2. We accept the solution for which Eqs. (24) and (26) are satisfied as being the more physically realistic one out of all possible solutions satisfying the Rankine-Hugoniot relations.

The entropy conditions assert that a shock solution is formed when the characteristics carry information towards the shock. Figure 4 shows that the curves showing the connections generated from the upstream state, $(h_{_-}, (\phi_0)_{_-}) = (1, 0.3)$ and the downstream state, $(h_{_+}, (\phi_0)_{_+}) = (0.1, 0.3)$ intersect at two distinct points. The latter are intermediate locations which are connected through a shock to the left state upstream and to the precursor states downstream. We are interested in determining how the characteristics at the leftmost and rightmost points compare to the speeds of the 1-shock and 2-shock waves, using the entropy conditions given by (26). For the case shown in Fig. 4, the eigenvalues at the left are computed as $\lambda_{1l} = 0.07, \lambda_{2l} = 0.19$ while at the right, these are $\lambda_{1r,} = 7.2 \times 10^{-4}, \lambda_{2r} = 1.9 \times 10^{-3}$.

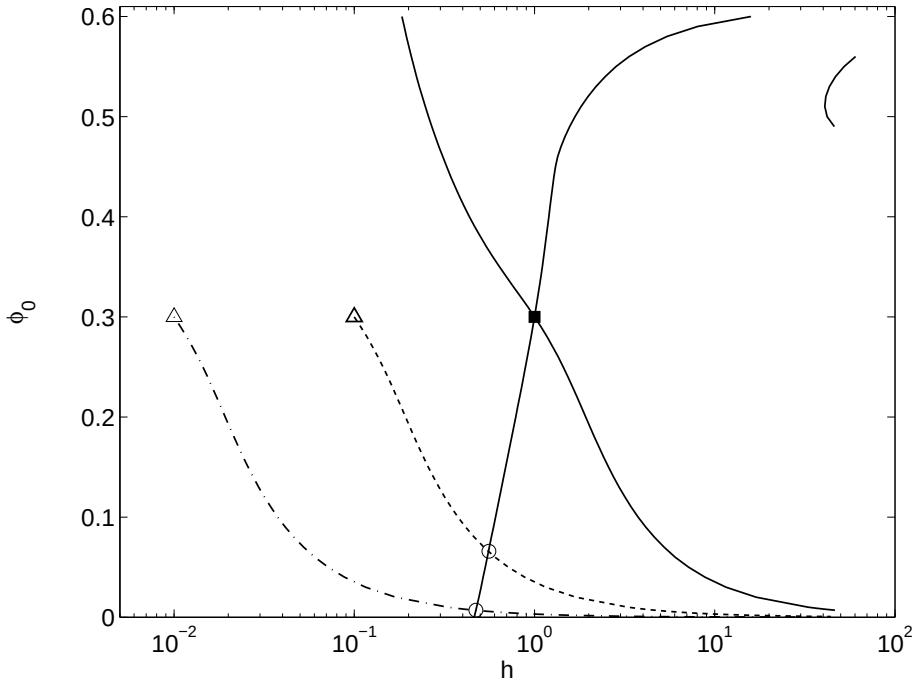

Fig. 5 The Rankine-Hugoniot locus calculated using Eq. (25) showing all shock connections (solid lines) from an upstream state $(h_-, (\phi_0)_-) = (1, 0.3)$ (▲) and two precursor states: $(h_+, (\phi_0)_+) = (0.1, 0.3)$ and $(h_+, (\phi_0)_+) = (0.01, 0.3)$, both shown with a hollow triangle marker. The dashed and dot-dashed lines represent 2-shock connections from $(h_+, (\phi_0)_+) = (0.1, 0.3)$ and $(h_+, (\phi_0)_+) = (0.01, 0.3)$, respectively. The intersection points show the possible intermediate states with the upstream state, calculated as $(h_i, (\phi_0)_i) = (0.56, 0.065)$ and $(h_i, (\phi_0)_i) = (0.46, 6.7 \times 10^{-4})$, both shown with a hollow round marker.

The 1- and 2-shock speeds are determined using any of the two relations in Eqs. (24); for the intermediate state indicated by a hollow, square marker in Fig. 4, the speeds are calculated as $s_1 = 0.05$ and $s_2 = 0.08$ for the 1-shock and 2-shock, respectively, while the characteristics are computed as $\lambda_{1i}, = 7.4 \times 10^{-4}, \lambda_{2i} = 2 \times 10^{-3}$. The speeds associated with the second intermediate state indicated by a round, hollow marker in the same figure, are computed as $s_1 = 0.07$ and $s_2 = 7.6 \times 10^{-4}$ while the characteristics are $\lambda_{1i} = 7 \times 10^{-4}, \lambda_{2i} = 1.9 \times 10^{-3}$. For a 2×2 system, the entropy conditions in (26) are expressed as follows; for the 1-shock,

$$\begin{aligned} \lambda_1(\boldsymbol{U}_l) > s_1 > \lambda_1(\boldsymbol{U}_i); \\ s_1 < \lambda_2(\boldsymbol{U}_i), \end{aligned} \tag{27}$$

and, for the 2-shock,

$$\begin{aligned} \lambda_1(\boldsymbol{U}_i) > s_2 > \lambda_1(\boldsymbol{U}_r); \\ \lambda_1(\boldsymbol{U}_i) < s_2. \end{aligned} \tag{28}$$

The characteristics at the three states and the shock speeds associated with each intermediate state show that both entropy conditions (27) and (28) are satisfied for $(h_i, (\phi_0)_i) = (0.56, 0.065)$ indicating that the solution is admissible. For the second intersection point, $(h_i, (\phi_0)_i) = (0.23, 0.53)$, while the 1-shock condition [Eq. (27)] is satisfied, the 2-shock condition [Eq. (28)] is violated. The admissible solution obtained as a result of the connection curves matches our observations in numerical simulations

where, for certain system parameters, we observe that the initial profiles for h and ϕ_0 evolve into a two-shock solution where the fixed states at the left and right boundaries are connected through an intermediate flat state.

In the above-mentioned examples, the fixed states for h were chosen such that $h_- > h_+$ where we showed, through the Rankine-Hugoniot relations, that shock connections exist for the particular set of left and right states. Like scalar conversation laws, it is possible to obtain smooth solutions of the PDE system which take the form $\boldsymbol{U}(x,t) = \boldsymbol{V}(x/t)$; these are known as rarefaction waves. For a 2×2 system, depending on the values of the fixed, boundary states, the solution may be represented by combinations of shock and rarefaction waves. In what follows we show that, for situations wherein the values of the right states are higher than the left states, the solution is described by shocks and rarefaction waves connected through intermediate states. Phase diagrams showing information on shocks (given by the Rankine-Hugoniot loci) and rarefactions (given by rarefaction integral curves) may be used to deduce interactions between shock-rarefaction solutions. In order to mathematically define the nature of rarefaction waves, we discuss the scale invariance of the problem. Under the transformation $(x,t) \to (\theta x, \theta t)$ (for any $\theta > 0$), we look for a self-similar solution $\boldsymbol{V}(\xi)$ where $\xi = x/t$. Given Eqs. (21) and (23), the self-similar solution should satisfy the following ordinary differential equation

$$-\xi \boldsymbol{V'} + f(\boldsymbol{V})' = 0, \tag{29}$$

and the boundary conditions,

$$\boldsymbol{V}(-\infty) = \boldsymbol{V}_-, \qquad \boldsymbol{V}(+\infty) = \boldsymbol{V}_+; \tag{30}$$

where the primes in Eq. (29) denote differentiation with respect to ξ. Rarefaction waves are constructed from self-similar solutions of the ODE (29) by solving

$$\boldsymbol{V}'(\xi)[J(\boldsymbol{V}) - \xi \boldsymbol{I}] = 0. \tag{31}$$

In Eq. (31), ξ is an eigenvalue of $J(\boldsymbol{V})$ and $\boldsymbol{V}'(\xi)$ is the corresponding eigenfunction. Next, we obtain rarefaction wave curves in the h-ϕ_0 phase space (as previously carried out for the construction of the shock wave curves shown in Figs. 3-5) by solving the above-mentioned eigenvalue problem. For a given initial condition, the objective is to start at the leftmost eigenvalue, obtain solutions to the ODE system such that a solution exists until ξ is equal to the rightmost eigenvalue. Such solutions, known as integral curves, give all the points $\boldsymbol{V}$ which can be connected to a set of fixed states, say $\boldsymbol{V}_-$, through rarefaction wave curves.

From Eq. (31), we can write down the conditions for a rarefaction wave solution as follows,

$$\begin{pmatrix} \lambda_i - h^2(3f - \phi_0 f') & -h^2 f' \\ -h^2(3g - \phi_0 g') & \lambda_i - h^2 g' \end{pmatrix} \begin{pmatrix} h_\xi \\ (h\phi_0)_\xi \end{pmatrix} = \begin{pmatrix} 0 \\ 0 \end{pmatrix}; \tag{32}$$

where we have used the Jacobian matrix given by Eq. (22) and λ_i denotes the eigenvalue with $i = 1$ for the leftmost and $i = 2$ for the rightmost eigenvalue. Equation (32) yields two coupled ODEs for the system of conservation laws; however, since λ_i is an eigenvalue of the system only one of the two equations is required to obtain the eigenfunction. Using the first equation, the resulting ODE gives a relationship between h_ξ and $(h\phi_0)_\xi$

$$[\lambda_i - h^2(3f - \phi_0 f')]h_\xi - h^2 f'(h\phi_0)_\xi = 0, \tag{33}$$

which ultimately yields,

$$\frac{dh}{d(h\phi_0)} = \frac{h^2 f'}{\lambda_i - h^2(3f - \phi_0 f')}. \tag{34}$$

Now, Eq. (34) may be integrated subject to a single initial condition, say $h = h_-$ at $h\phi_0 = (h\phi_0)_-$ to obtain solutions in the $h - h\phi_0$ phase plane; we opt to show these connections in the $h - \phi_0$ as the primitive variables represent the physical meaning more clearly. Further, we note that, if a solution exists, the leftmost eigenvalue yields all points $\boldsymbol{V}$ which connect to the left states through a 1-rarefaction wave while the rightmost eigenvalue similarly gives us solutions which connect to the left state through a 2-rarefaction wave.

In Fig. 6, we show admissible Rankine-Hugoniot loci from two boundary states: (1,0.3) shown by a square marker, and (0.1,0.1) shown by a hollow, triangle marker. 1-shock connections from (1,0.3) are represented by solid, black lines (here, 2-shock connections are inadmissible and therefore not shown). Further, 1- and 2-shock connections are plotted from (0.1,0.1) represented by black, dashed lines. Figure 6 also depicts 1- and 2- rarefaction wave curves from (1,0.3), represented by thick, gray, dot-dashed lines. We note that the 1-shock and 1-rarefaction curves from (1,0.3) completely overlap. Additionally we mark two intersection points (shown by solid circle and solid triangle markers) on the plot both of which represent possible solutions depending whether the above-mentioned fixed points represent upstream or downstream states. We start with the case wherein (1,0.3) is an upstream state where we observe that the 1-shock/1-rarefaction curve from the upstream state intersects with the 2-shock curve from the downstream state at (0.49,0.02), indicated by the solid, triangle marker. We now discuss the case wherein (1,0.3) is a downstream boundary point. The curves which intersect are the 1-shock connections from the upstream and the 2-rarefaction curve from the downstream state. Thus, the solution is expected to be represented by a 1-shock, 2-rarefaction wave connected through an intermediate state at (0.2,0.4), indicated by a solid, circle marker.

In the next section, we discuss the numerical solutions obtained for the slurry thickness and particle volume fraction. Further, we indicate how the results from the shock and rarefaction analysis compare to the numerical simulations and physical experiments.

3.2 Numerical solutions

The film thickness and particle concentration equations are solved numerically in MATLAB using an up-wind scheme. We first formulate the initial-boundary-value problem. The latter consists of the system given by Eq. (21) and a set of initial and boundary conditions for the two dependent variables. We use two sets of initial conditions for h and ϕ (note that we denote the particle concentration by ϕ instead of ϕ_0 henceforth), both simulating a constant flux of particles and fluid onto the plane. Both sets of initial conditions assume a step-like profile for the initial height given as

$$h(x,0) = (h_- - h_+)u_c(-x) + h_+, \tag{35}$$

where u_c is the unit step function. Equation (35) holds true at $t = 0$ for all values of x. Physical experiments undertaken in the Applied Mathematics laboratory at UCLA simulate a constant *volume* scenario, where a finite volume of particles and oil are deposited on the plane and allowed to flow under gravity. The objectives of the current paper are devoted on the *Riemann* initial data for h for which the conservation laws are solved using initial constant piecewise data with a single discontinuity between the left and right boundaries. We choose to tackle the Riemann problem for situations wherein $h_- > h_+$ and $h_- < h_+$ in Eq. (35), representing a step-down and step-up function, respectively. This is shown in Fig. 7; the first Riemann problem is shown on the right of the dotted line where $h_- > h_+$ while the second Riemann problem is represented by $h_- < h_+$, shown on the left. We note that the local Riemann problems combined simulate the initialization of the physical experiments best. In what follows, the numerical simulations are solved either with a step-down or a step-up function. The left

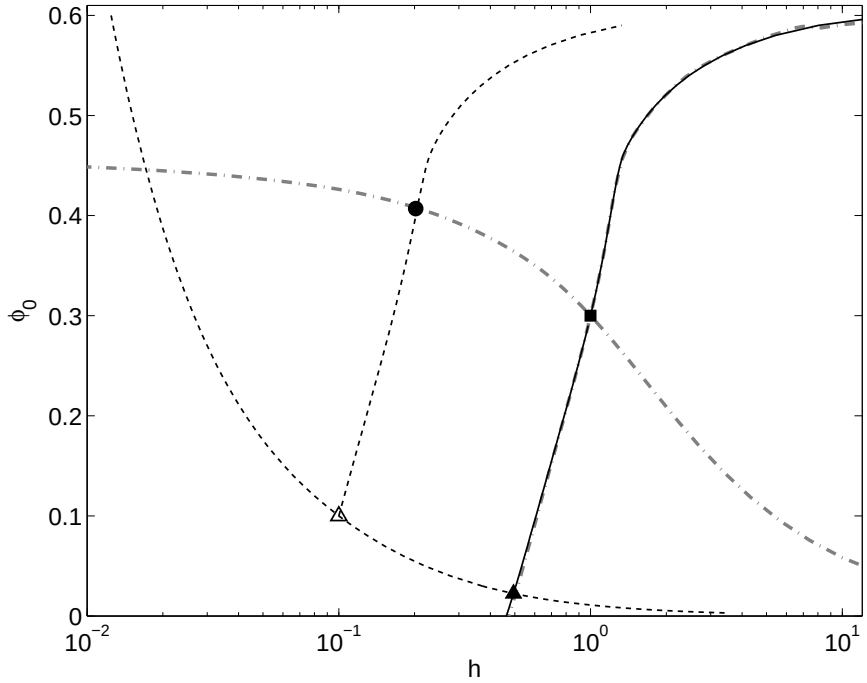

Fig. 6 Shock and rarefaction curves for the system. Here, the Rankine-Hugoniot locus calculated using Eq. (25) shows 1-shock connections (solid lines) from the fixed state $(1, 0.3)$ (■) and shock connections (dashed lines) from a second fixed state $(0.1, 0.1)$ (△). 1- and 2-rarefaction integral curves at $(1, 0.3)$ are shown by thick, dot-dashed, gray lines. We mark two intersection points: one given by the shock-shock connections (shown with a ▲) and another given by the shock-rarefaction connections (shown with a ●). We note that the 1-shock and 1-rarefaction curves for the state $(1, 0.3)$ overlap. Numerical simulations show that, starting with $(1, 0.3)$ as the upstream state give a shock-shock solution (see Fig. 8 for a representation of the numerical solution) while, starting with $(1, 0.3)$ as the downstream state the solution is described by a 1-shock, 2-rarefaction wave (see Fig. 14). The intersection points given by the markers ▲ and ● match the flat states shown in the numerical simulations in Figs 8 and 14, respectively.

and right boundary states for h satisfy $h_-, h_+ > 0$; this is done to overcome the modeling difficulties associated with the behavior of the front at the contact line, when $h = 0$. We consider two scenarios to initialize the particle volume fraction equation: in the first one, ϕ is chosen to be uniform across all x [see Eq. (36)] while in the second one, a step-like profile is chosen for ϕ [see Eq. (37)]:

$$\phi(x, 0) = \phi_-, \tag{36}$$

$$\phi(x, 0) = (\phi_- - \phi_+)u_c(-x) + \phi_+; \tag{37}$$

in both Eqs. (36) and (37), ϕ_- represents a fixed upstream concentration representing the initial particle volume fraction. Similarly to Eq. (35), the fixed states in Eq. (37) can lie within $\phi_- > \phi_+$ or $\phi_- < \phi_+$. For the step function given by (37), we note that, for $\phi_- > \phi_+$, the initial condition simulates a physical setting more closely, wherein the majority of the particles are found to be well mixed within the fluid behind the shock, while downstream of the shock, where the film is very thin, the distribution of particles is expected to be sparse. This is achieved via a step function where the precursor simulates a particle-free film as $\phi_+ \to 0$. Finally, at the boundaries, i.e. at $x = x_{_L}$ and $x = x_{_R}$, we demand that the left and right states for h and ϕ are satisfied for all time t,

$$h_x(x_{_L}, t) = h_x(x_{_R}, t) = 0 \ \text{ and } \ \phi_x(x_{_L}, t) = \phi_x(x_{_R}, t) = 0. \tag{38}$$

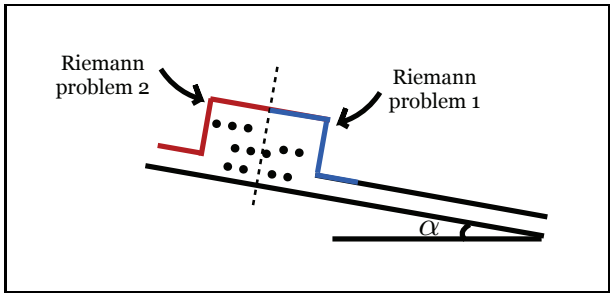

Fig. 7 Initialization of numerical simulations. We tackle two Riemann problems to identify all shock and rarefaction connections for the 2×2 system of conservation laws. In 'Riemann Problem 1' $h_- > h_+$ while in 'Riemann Problem 2', $h_- < h_+$. The initial conditions for the particle volume concentration vary from a uniform concentration along all x to a step-up or step-down function similar to the two Riemann problems shown in this figure.

We note that we obtain numerical solutions for the conserved variables h and $h\phi$ but, for clarity, we choose to present the results separately for the fluid interface and particle volume fraction in all figures in this section. In all the numerical simulations presented in this paper, we fix the plane angle of inclination at $\alpha = 30^o$. Further, in order to simulate best the experiments carried out in our laboratory, we choose a relative density equal to $\rho_s = 1.5$, which is calculated using the densities of negatively buoyant glass beads and silicon oil. The constants C_1 and C_2 defined earlier are calculated as 1.02 and 1.45, respectively.

It has been shown [1, 15] that the numerical simulation of the system of equations presented in the current paper generates different types of solutions depending on the choice of system parameters. The latter refer to the left and right states for h and ϕ, corresponding to a fixed, constant in-flux and out-flux of fluid and particles, respectively. Additionally, the plane angle of inclination, α may be adjusted, which in turn affects the velocity distribution within the slurry. It is noted that the initial particle volume fraction is set by the upstream or left state imposed on ϕ. For low initial particle concentrations i.e. $\phi_- < \phi_c$ and low inclination angles, the particles settle rapidly allowing clear fluid to flow over them. As previously mentioned, this is referred to as the 'settled' regime which has been observed in monodisperse, particle-laden flow experiments. Figure 8 shows the evolution of h and ϕ starting from Eq. (35) for h and, from Eq. (36) [panel (a)] and Eq. (37) [panel (b)] for ϕ. For low initial concentrations, i.e. $\phi_- < \phi_c$ the solution in both h and ϕ is described by a shock connecting the preset left and right states through intermediate states, as shown in Fig. 8; it is noted that initial concentrations within $\phi_- < \phi_c$ correspond to the lower part of the phase diagram in Fig. 2(a). The intermediate state observed in the simulations in Fig. 8 match the shock-shock intersections shown in the phase plots in Fig. 5 [for panel (a)] and Fig. 6 [for panel (b)]. A pictorial evolution of the flow regime is shown in Fig. 9 showing the separation of particle-rich and particle-free regions.

Figure 10 shows the solutions for high initial particle concentrations, $\phi_c < \phi_- < \phi_{\max}$; here, we use $\phi_- = 0.5$. In the case of uniform particle concentration along the x-axis [panel (a)], at $t = 2000$, the solution is described by a sharp increase in the height profile which forms a ridge resembling a singular shock; details for the theory behind the formation of these singular shocks can be found in the work of Wang and Bertozzi [22]. The insert in panel (a) depicts a magnified view of the concentration profile showing that the initial concentration increases to a value approaching that of maximum packing, $\phi_{\max} = 0.61$. The increase in ϕ corresponds to the ridge in h suggesting that a greater number of particles accumulates at the ridge. This pattern has been associated with the so-called 'ridged' regime observed experimentally [see Fig. 11 for a pictorial evolution of this regime] wherein the particles move towards the front of the flow and aggregate at the contact line. If the simulation is initiated with the

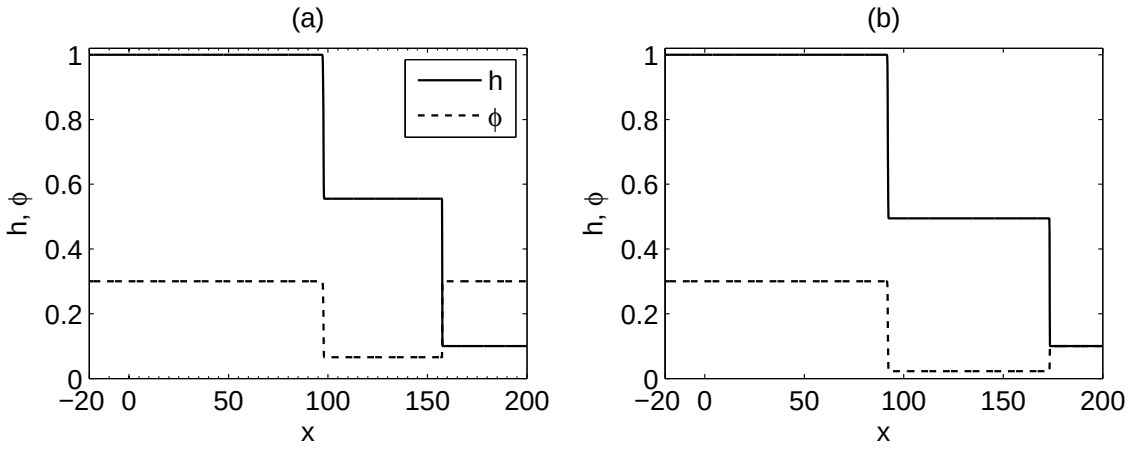

Fig. 8 Numerical solution of the film thickness (solid line) and the particle volume fraction (dashed line) at $t = 2000$. In both panels, the left and right states are chosen as $h_- = 1$ and $h_+ = 0.1$, respectively and the left state for ϕ is 0.3. In panel (a) the initial condition for ϕ is given by Eq. (36) and in (b), we use Eq. (37) with $\phi_+ = 0.1$. Here, the domain length is $\mathcal{L} = 220$ and the mesh size used is $dx = 0.1$.

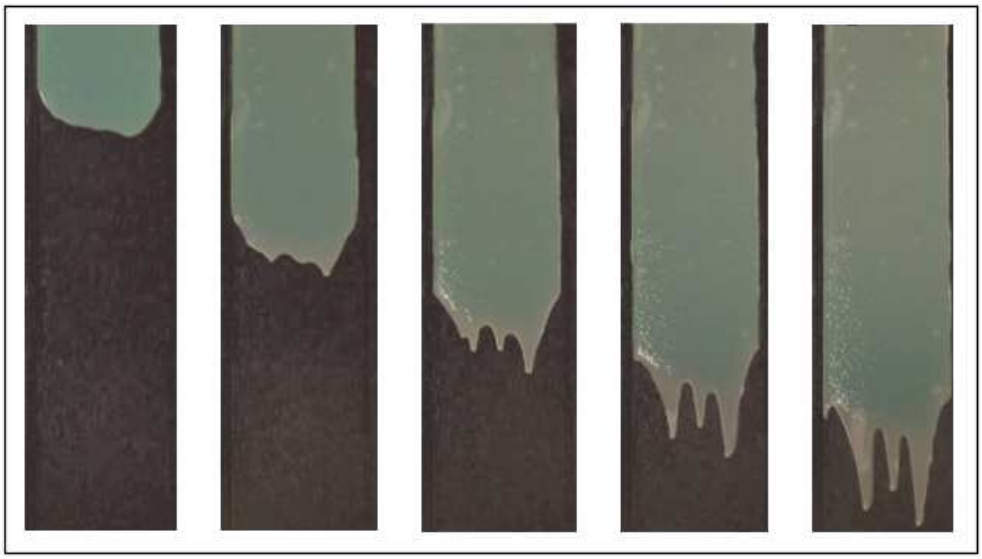

Fig. 9 Pictorial evolution of the 'settled' regime showing the particles settling while clear fluid flows over the particles resulting in the formation of fingers. The plane angle of inclination is set to 30^o while the particle concentration is chosen as 0.25. The first snapshot is shown 30 seconds after the onset of the experiment while the last one is shown after 3 minutes. The color of the inclined plane has been darkened to clearly show the contrast between the particle-rich region (light blue) and the clear fluid fingers.

step profile in ϕ however, the solution is described by intermediate states connecting the left and right fixed positions in h and ϕ. This result is similar to the one observed in lower initial concentrations; however in Fig. 10(b), the particle-free region is observed to be much shorter. In the case shown in Fig. 10, the initial particle concentration exceeds the critical value, corresponding to the upper part of the phase diagram shown in Fig. 2(a).

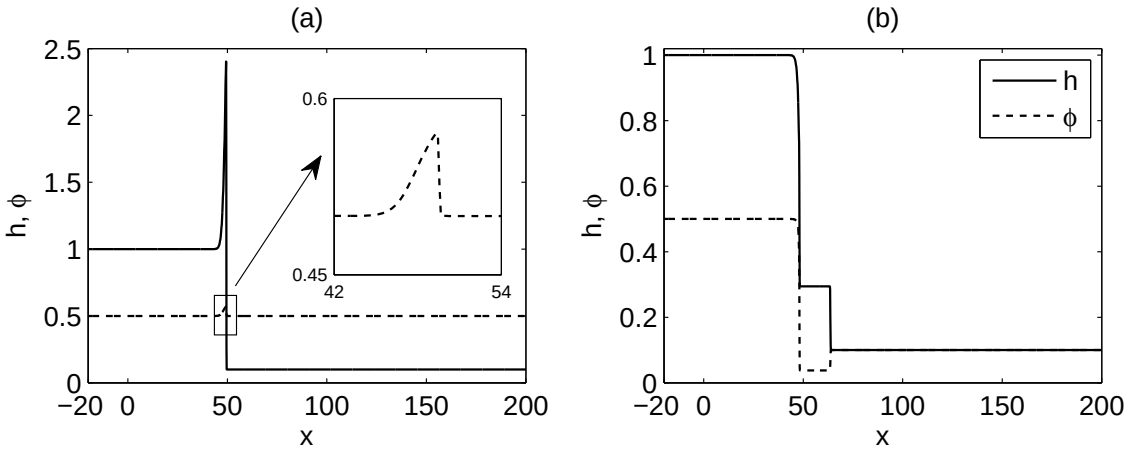

Fig. 10 Numerical solution of the film thickness (solid line) and the particle volume fraction (dashed line) at $t = 2000$. In both panels, the left and right states are chosen as $h_- = 1$ and $h_+ = 0.1$, respectively and the left state for ϕ is 0.5. In panel (a) the initial condition for ϕ is given by Eq. (36) and in (b), we use Eq. (37) with $\phi_+ = 0.1$. The insert in panel (a) shows a magnified region of the concentration profile. The rest of the parameters remain unchanged from Fig. 8.

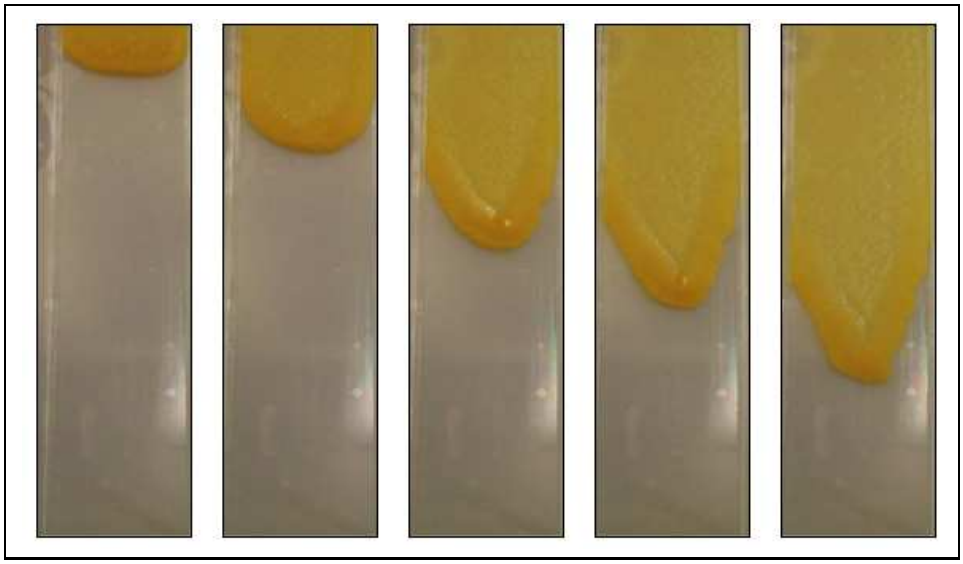

Fig. 11 Pictorial evolution of the 'ridged' regime. As the slurry flows down the plane, the particles rapidly aggregate at the contact line forming a particle-rich ridge. The plane angle of inclination is set to 30^o while the particle concentration is chosen as 0.5. The first snapshot is shown 1 minute after the onset of the experiment while the last one is shown after 26 minutes.

Figure 2(a) suggests there exists a local bifurcation at the critical ϕ_c [calculated using Eq. (17)] which represents an unstable, flat state. Using Eq. (17) and, for the parameter values outlined in Section 2, this critical state is calculated as $\phi_c = 0.459$. Next, we start the numerical simulations with an initial particle concentration equivalent to the critical value; the solutions are shown in Fig. 12. In panel (a), where ϕ is initially uniform across x, the solution does not form shock connections between the

prescribed states at the boundaries at the chosen, final simulation time of $t = 2000$. Instead, one gets a single shock solution for special case ϕ_c. This critical value satisfies the overdetermined system given by Es. (24). In panel (b), the initial step profiles in both variables form intermediate shocks connecting the left and right states, as observed in Figs. 8(b) and 10(b).

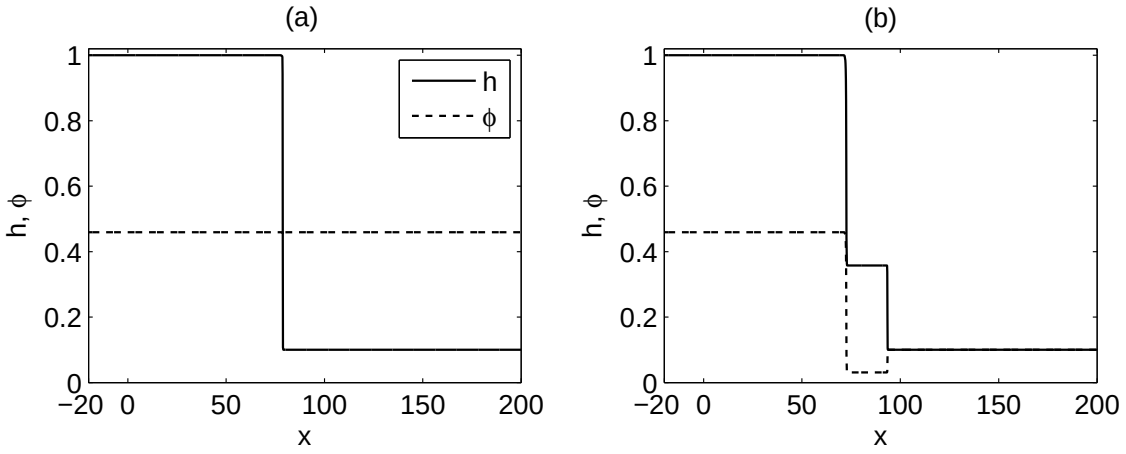

Fig. 12 Numerical solution of the film thickness (solid line) and the particle volume fraction (dashed line) at $t = 2000$. In both panels, the left and right states are chosen as $h_- = 1$ and $h_+ = 0.1$, respectively and the left state for ϕ is 0.4593, which is equivalent to the critical concentration, ϕ_c according to Eq. (17). In panel (a) the initial condition for ϕ is given by Eq. (36) and in (b), we use Eq. (37) with $\phi_+ = 0.1$. Here, the domain length is $\mathcal{L} = 220$ and the mesh size used is $dx = 0.1$.

It is of interest to identify whether the flat state, shown in Fig. 2(a) 'selects' one of the two above-mentioned regimes, 'settled' or 'ridged', when the numerical simulation is allowed to run over a long time. We find that for an initial concentration equal to the critical value, the interfacial solutions lack the formation of any shocks or waves at the interface, even at long times.

It is clear from Fig. 10 that, for an initial particle volume fraction exceeding the critical value, the existence of the singular shock depends on the initial distribution of ϕ along x. In Fig. 10(a) where $\phi_- = \phi_+$, a singular shock develops indicating a high volume of particles at the ridge, while in Fig. 10(b), the solution indicates that the particles are mostly concentrated in the fluid region upstream of the shock. In Fig. 13, we start the numerical simulations using Eqs. (35) and (37) with $h_- = 1$, $h_+ = 0.1$, $\phi_- = 0.5$ and, gradually increase the right state for ϕ from 0.40 to 0.46, in increments of 0.02; this is shown in panels (a)-(d). The final time for the solutions shown in all four panels is fixed at $t = 2550$. The solution in panels (a)-(c) is described by a jump between the left and right states, connected by an intermediate state. If the jumps are shocks, then, through the Rankine-Hugoniot locus, we can determine the connection between the two states at the left and right boundaries. It is observed that, as ϕ_+ is increased, the domain over which the flat state develops, decreases [see panels (a)-(c)]. As ϕ_+ is increased further, we observe a transition to the singular shock connecting the states at the two boundaries. The transition occurs when the right state for ϕ is sufficiently close to the left state, $\phi_- = 0.5$. We observe that, for high particle volume fractions and, while the solution is still described by jumps [panels (a)-(c)], the numerical solutions exhibit notable numerical diffusion; the error was found to be reduced with an increase in the mesh density.

In the case of singular shocks, the speed of the shock is no longer defined by the classical Rankine-Hugoniot jump condition; the singular shock observed is described as the weaker solution to Eqs. (21),

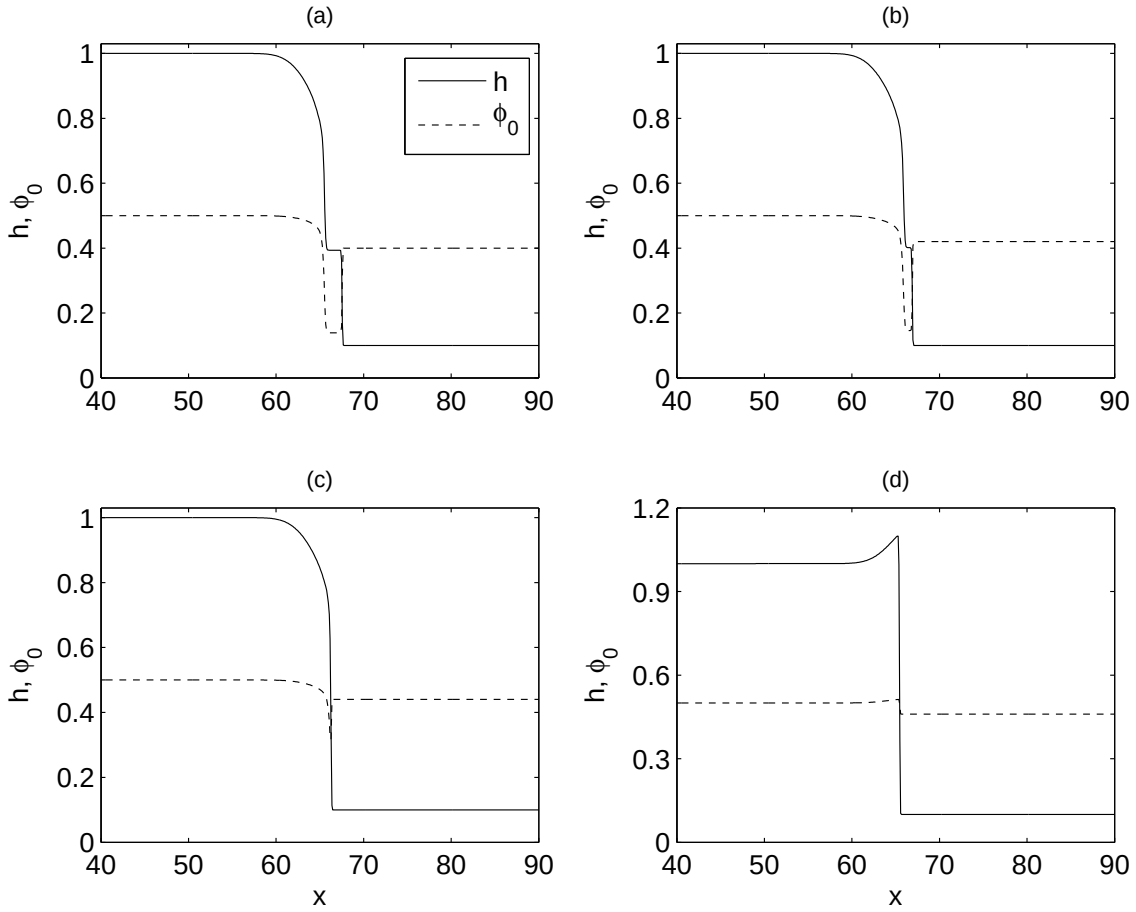

Fig. 13 Numerical solution of the film thickness (solid line) and the particle volume fraction (dashed line). In all panels the solutions are shown at $t = 2550$ while the left and right states for h are chosen as $h_- = 1$ and $h_+ = 0.1$, respectively and the left state for ϕ_- is fixed at 0.5. In Eq. (37), ϕ_+ is increased from 0.40 to 0.46, in 0.02 increments in panels (a) to (d). Here, the domain length is $\mathcal{L} = 120$ and the mesh size used is $dx = 0.1$.

as shown in the work of Cook *et al.* [23] where the authors employed a continuum model for gravity-driven, particle-laden flows. As evident from the numerical solutions shown in Figs. 12(a) and 13(d), a distribution solution for the conserved variables $\boldsymbol{U} = (h, h\phi)$ may be expressed as,

$$\boldsymbol{U}(x,t) = M_{\boldsymbol{U}}(t)\delta(x - st) + \begin{cases} \boldsymbol{U}_- & \text{if } x < st \\ \boldsymbol{U}_+, & \text{if } x > st \end{cases} \tag{39}$$

where $M_{\boldsymbol{U}}(t) = (M_h(t), M_{(h\phi)})$ denote the mass accumulation in h and $h\phi$ at $x = st$ and $\delta(x - st)$ is the Dirac delta function; the principle of conservation of mass allows us to express the growth rate as follows

$$\begin{aligned} \frac{dM_h}{dt} &= s_s(h_- - h_+) - [F_- - F_+], \\ \frac{dM_{h\phi}}{dt} &= s_s[(h\phi)_- - (h\phi)_+] - [G_- - G_+]; \end{aligned} \tag{40}$$

where, s_s is the speed of the singular shock and F and G are the fluxes, defined in previous sections. Following [22], by making use of the following simple constitutive relation $M_{(h\phi)} = \phi_{\max} M_h$, we solve for the unknown shock speed,

$$s_s = \frac{\phi_{\max}[F_+ - F_-] - [G_+ - G_+]}{(h_+ - h_-)\phi_{\max} - [(h\phi)_+ - (h\phi)_-]}. \tag{41}$$

Wang and Bertozzi [22] have shown that the formation of the singular shock depends on the thickness of the precursor and the initial particle concentration. The authors have specifically shown that as the precursor height is varied and while the solution is still represented by a double-shock, the two shock speeds approach each other until the two speeds coincide (at a particular value of h_+) at the onset of the singular shock transition; thereafter the speed of the singular shock is described by Eq. (41).

In Fig. 14, we plot numerical solutions for h and ϕ against x [panels (a), (b)] at different times t, where the system parameters are the same as in Fig. 8(b); however in Fig. 14, the left and right states have been reversed. Perhaps the most distinct feature of the solutions in h and ϕ is the formation of a smooth solution emerging from the rightmost state. Following the rarefaction wave theory discussed in Subsec. 3.1, we plot the evolution of the solutions in h and ϕ against the rescaled variable $\xi = x/t$ in panels (c) and (d), respectively. From panels (c) and (d), we observe the self-similarity of the h and ϕ profiles as the late time solutions, collapse onto one curve showing the formation of a shock solution (1-shock) and a rarefaction wave (2-rarefaction). The shock solution connects the left, fixed state to an intermediate state which then connects to the right, fixed state through a rarefaction wave. The intermediate state is extracted from the numerical solution to be (0.2,0.4) which matches the intersection of the 1-shock, 2-rarefaction curves shown in the phase diagram in Fig. 6 by a solid, circle marker.

Next, we examine the evolution of the film thickness and particle volume fraction, initialized with a step-up function for h with $h_- = 0.1$ and $h_+ = 1$ and a high, uniform particle concentration equal to 0.5. The final time solution is shown in Fig. 15 at $t = 12750$, plotted against the rescaled variable ξ. The inserts in panels (a) and (b) show a magnified region of the intermediate states in h and ϕ, respectively, which in this case are lower than the preset left states. This implies a thinning of the film associated with a low particle concentration in the vicinity of the leftmost boundary while downstream of the intermediate state, a smooth increase is observed both in the film thickness and the concentration of the particles. The solution in the entire ξ domain appears to be smooth; in Fig. 16 we plot the admissible 1-shock and 1-rarefaction loci from the left state (0.1,0.5) and the admissible 2-rarefaction locus from the right state (1,0.5). We observe total overlap of the 1-shock and 1-rarefaction curves emerging from (0.1,0.5) [also observed in Fig. 6]. The overlapped 1-shock, 1-rarefaction curves intersect with the 2-rarefaction curve from (1,0.5), indicated by the solid, circle marker in Fig. 16. The intersection point represents the intermediate state observed in the numerical simulation depicted in Fig. 15. It is noted that the 2-shock connections from (1,0.5) failed to intersect with any connection loci from the left state, indicating the lack of an admissible connection, and are therefore not shown in the phase diagram.

4 Concluding remarks

This paper focuses on the theoretical modeling of thin-film, particle-laden flows in the presence of contact lines flowing under the action of gravity on an inclined plane. The model employed has been previously derived [1, 15] using the lubrication approximation on the Stokes equations, continuity and particle transport equation, to capture the dominant physics in this fluid flow setting. We focus on the

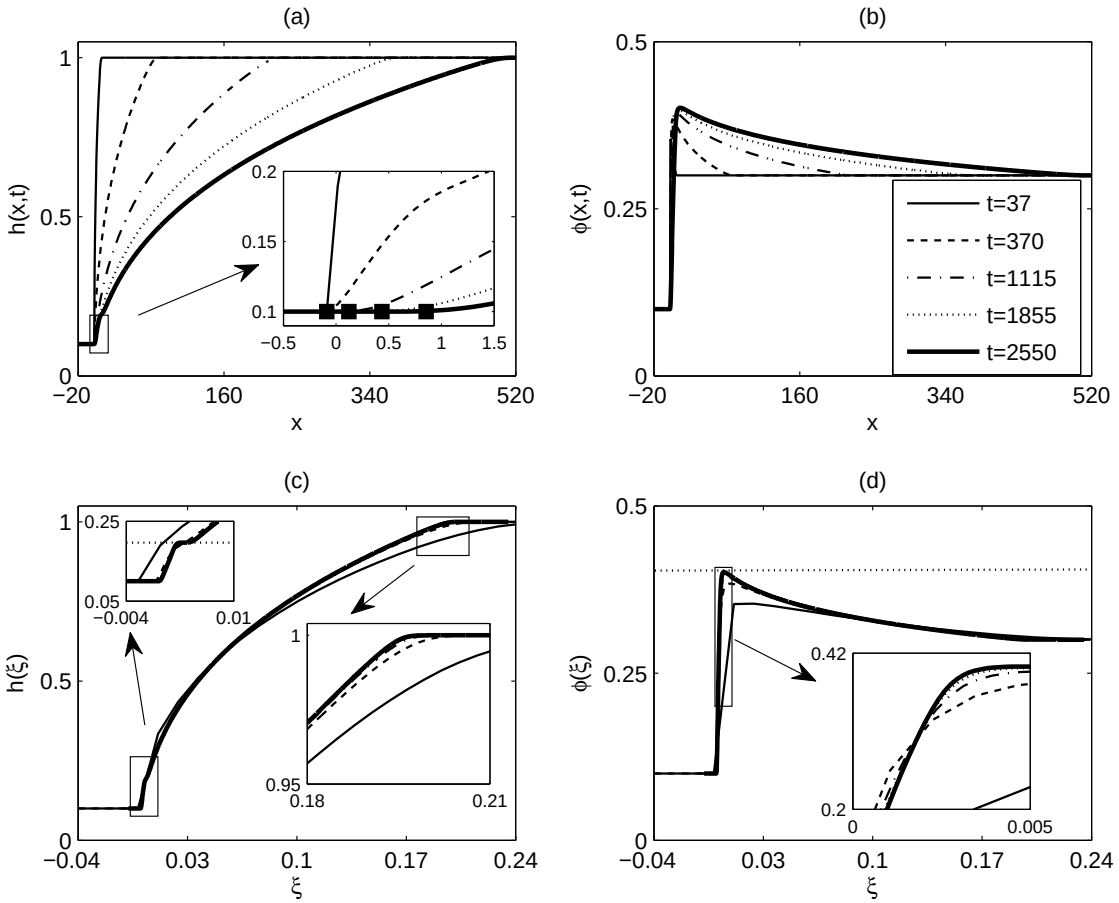

Fig. 14 Numerical simulations showing the evolution of h [panel (a)] and ϕ [panel (b)] starting from Eqs. (35) and (36) for h and ϕ, respectively. The left states are chosen as $(0.1, 0.1)$ and the right states as $(1, 0.3)$; the averaged particle volume fraction is fixed at 0.1 at the left boundary. The final solution time is shown with a thick, solid line at $t = 2550$ while the legend in panel (b) shows the times for all the soluti2ons. From left to right, the square markers shown in the insert in panel (a) illustrate that the x-position of the upstream shock is advancing in x with time, albeit rather slowly. Panels (c) and (d) depict plots of the film thickness and the particle volume fraction, respectively, against the rescaled variable $\xi = x/t$ showing the formation of a 1-shock and a 2-rarefaction wave; the latter is indicated by the complete overlap of the late-time solutions.The different line types correspond to the legend shown in panel (b). The leftmost insert in panel (c) depicts the formation of the intermediate state connecting the shock and rarefaction wave where the horizontal, dotted line shows that the intermediate value for h is at $h = 0.2$. The intermediate state for ϕ is shown in panel (d) with a horizontal, dotted line at $\phi = 0.4$.

analysis of a system of 2×2 conservation laws utilizing the mathematical theory of shock solutions and rarefaction waves. We show that, depending on the amount of particles initially mixed with the fluid and the initial distribution profile of the particles, the solutions may be described by double shocks, rarefaction-shock waves or singular shocks. In this study, we focus on a constant flux scenario for the slurry in which we simulate a continuous in-flux and out-flux of fluid and particles onto the inclined plane using Riemann initial data for h. We investigate the effect of two initial conditions for h: a step-down function where the film is thick upstream and the precursor is kept thin or a step-up function where the reverse is true [see Fig. 7]. The current paper focuses on identifying all

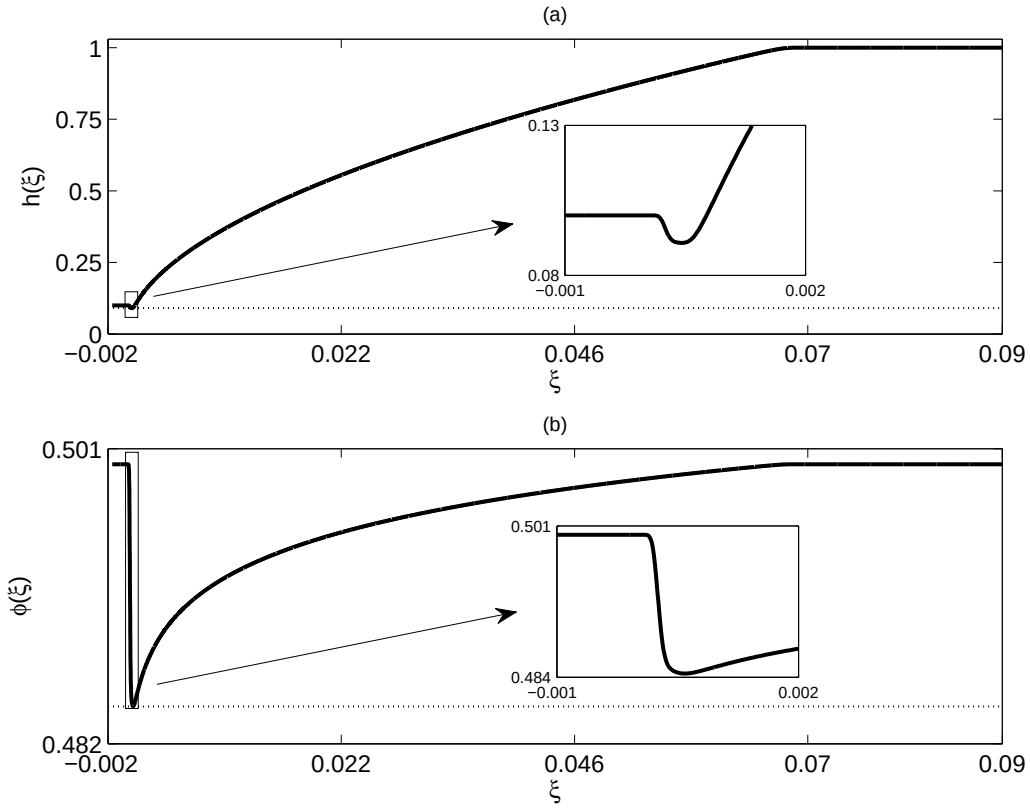

Fig. 15 (a) Numerical solution of the film thickness at $t = 12750$ plotted against the rescaled variable $\xi = x/t$. The solution is represented by a 1-shock (or 1-rarefaction) and 2-rarefaction wave. The left and right states are fixed at $(h_-, \phi_-) = (0.1, 0.5)$ and $(h_+, \phi_+) = (1, 0.5)$, respectively. The horizontal dotted line represents the intermediate state in h calculated as $h_i = 0.09$. (b) The evolution of the particle volume fraction solution at the final time solution of $t = 12750$ showing the formation of the intermediate state (indicated by a horizontal, dotted line). This is calculated as $\phi_i = 0.484$ then connects to the right state though a 2-rarefaction wave. Note that the values of the latter, downstream of the intermediate state increase smoothly as the solution approaches the right boundary fixed state.

possible entropy conditions by studying the two local Riemann problems. For the particle volume concentration, we choose to initialize the simulations through (i) a uniform particle concentration along the x-axis of the plane and (ii) a step-up or step-down profile indicating that the majority of the particles are found in regions where the film is thick. Numerical results include compressive, double-shock solutions connecting the left and right states through an intermediate state whose value is shown to match the classical shock theory. The latter involves identifying admissible shock connections which are predicted by the Rankine-Hugoniot jump relations and satisfy the entropy conditions. In numerical simulations we observe that, with increasing total particle concentration, the solution changes from the double-shock structure to singular shocks; these are characterized by large, local peaks in the film height corresponding to a high particle volume fraction approaching maximum packing. Such profiles have been observed experimentally for initially highly packed slurries where the majority of particles accumulate at the front of the flow forming a particle-rich ridge. Further, the existence of smooth solutions represented by rarefaction waves, was found in cases where a step-up profile is employed as the initial condition for h and ϕ such that the value on the right boundaries exceed

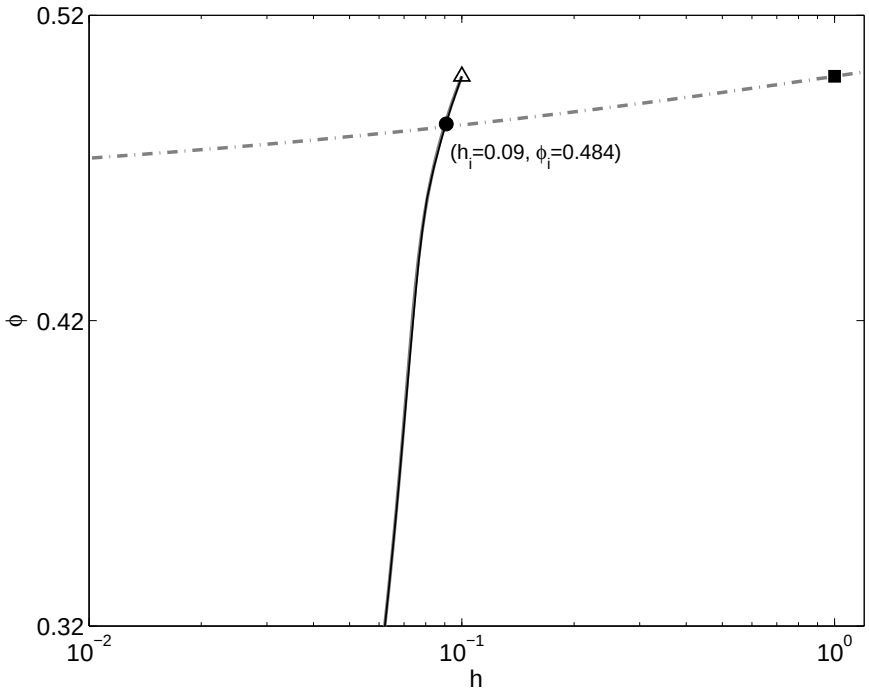

Fig. 16 Shock and rarefaction connections for the system with fixed states (0.1,0.5) (△) and (1,0.5) (■). Admissible shock connections from △ are shown with black, solid lines while the rarefaction curve from the same state is shown with a thick, gray line (this completely overlaps the thin, black solid line of the aforementioned shock connection). 2-rarefaction curves from ■ are shown with a thick, gray, dot-dashed line. The circle marker represents the intersection point between the overlapped 1-shock/1-rarefaction curves from △ and the 2-rarefaction curve from ■); this matches the numerical simulation result shown in Fig. 15.

those on the left. Self-similar solutions depict that the rarefaction waves collapse onto a single curve with increasing simulation time. The construction of a phase diagram showing admissible shock and rarefaction connections assert that the numerical solutions are represented by shock-rarefaction or rarefaction-rarefaction waves.

Acknowledgements

This work was supported by UC Lab Fees Research Grant 09-LR-04-116741-BERA and NSF grants DMS-1048840, DMS-0968309 and DMS-1045536. The authors would like to acknowledge Dr. Li Wang and Dr. Sungyon Lee for helpful conversations.

References

1. N. Murisic, J. Ho, V. Hu, P. Latterman, T. Koch, K. Lin, M. Mata, A.L. Bertozzi, Physica D: Nonlinear phenomena **240** (2011)
2. H.E. Huppert, Nature **300**, 427 (1982)
3. A. Oron, S.H. Davis, S.G. Bankoff, Rev. Mod. Phys. **69**, 931 (1997)
4. J. Sur, A.L. Bertozzi, R.P. Behringer, Phys. Rev. Lett. **90**, 126105 (2003)
5. R.V. Craster, O.K. Matar, Rev. Mod. Phys. **81**, 1131 (2009). DOI 10.1103/RevModPhys.81.1131
6. G.J. Kynch, Transactions of the Faraday society **48**, 166 (1952)
7. J.F. Richardson, W.N. Zaki, Chem. Eng. Sci. **3**, 65 (1954)
8. R.H. Davis, A. Acrivos, Ann. Rev. Fluid Mech. **17**, 91 (1985)
9. J.J. Zhou, B. Dupuy, A.L. Bertozzi, A.E. Hosoi, Phys. Rev. Lett. **94**, 117803 (2005)
10. A.L. Bertozzi, M.P. Brenner, Phys. Fluids **9**, 530 (1997)
11. J.A. Diez, L. Kondic, Phys. Rev. Lett. **86**, 632 (2001)
12. B.P. Cook, A.L. Bertozzi, A.E. Hosoi, SIAM J. Appl. Math. **68**, 760 (2007)
13. B.P. Cook, Phys. Rev. E **78**, 045303 (2008)
14. B.P. Cook, O. Alexandrov, A.L. Bertozzi, Eur. Phys. J. Special Topics **166**, 77 (2009)
15. N. Murisic, B. Pausader, D. Peschka, A.L. Bertozzi. Dynamics of particle settling and resuspension in viscous liquids. Under review for *J. Fluid Mech.*
16. L. Kondic, J.A. Diez, Phys. Fluids **13**, 3168 (2001)
17. A.L. Bertozzi, A. Münch, M. Shearer, Physica D **134**, 431 (1999)
18. J.C.V. der Werff, C.G.D. Kruif, J. Rheol. **33**, 3 (1989)
19. J.F. Brady, J. Chem. Phys. **99**, 567 (1993)
20. R.J. Phillip, R. Armstrong, R.C. Brown, A. Graham, J.R. Abbott, Phys. Fluids A **4**, 30 (1992)
21. P.D. Lax, Society for Industrial and Applied Mathematics **2**, 17 (1971)
22. L. Wang, A.L. Bertozzi. Shock solutions for high concentration particle-laden thin films. Submitted to SIAP (2013)
23. B.P. Cook, Lubrication models for particle-laden thin films. Ph.D. thesis, University of California, Los Angeles (2007)